$\int_{-1}^{1} F_{ts}(z + Au) T_n(u) du / \sqrt{1-u^2}$. With integration by parts (n times), we find that a_n is given by a weighted average of the nth derivative of F_{ts} (Eq. 1).
14. U. Dürig, *New J. Phys.* **2**, 5.1 (2000).
15. U. Dürig, *Appl. Phys. Lett.* **75**, 433 (1999).
16. S. Hembacher, thesis, Augsburg University, Augsburg, Germany (2003).
17. Because the coefficients of thermal expansion are greatly reduced at temperatures near absolute zero, the thermal drift (i.e., a slow drift of the probe with respect to the sample), a common nuisance in scanning probe experiments, is reduced to 25 pm/hour. The resulting accuracy and time stability permits measurements at very slow scanning speeds and in a constant-height mode, during which the z feedback can be turned off for at least 3 hours while remaining in the tunneling distance regime.
18. We attempted to prepare tips made of doped diamond, but the electrical conductivity of these tips was insufficient for simultaneous AFM/STM operation. Carbon nanotubes might also appear promising as AFM tips, but we require very stiff tips to avoid artifacts from elastic tip deflections.
19. H. Mizes, thesis, Stanford University, Stanford, CA (1987).
20. C. J. Chen, *Introduction to Scanning Tunneling Microscopy* (Oxford Univ. Press, New York, 1993).
21. F. J. Giessibl, *Appl. Phys. Lett.* **76**, 1470 (2000).
22. In our setup, f_0 is small compared with the bandwidth of the deflection detector. Hence, the higher harmonics can be measured with an excellent signal-to-noise ratio. The output voltage of the high-pass filter is given by $V_{hh} = (\sum_2^\infty (S_n a_n)^2)^{1/2}$, where S_n denotes the sensitivity of our deflection sensor for the nth harmonic with $S_n \approx n/(1 + 0.0767n^2)^{1/2} \times 0.1$ mV/pm. S_n is given by the product of the current per deflection generated by the force sensor [equation 2 in (*21*)] times the conversion rate of the preamplifier with $V/I = 10$ megaohms/$(1 + (f/f_{3\,dB})^2)^{1/2}$, where $f_{3\,dB} = 65$ kHz.
23. In addition to the tunneling current and higher harmonic signal, the frequency shift and the dissipation signal were recorded in parallel (*43*). The frequency shift data are similar to the higher harmonic data in the right column of Fig. 2, yet with much less contrast and a substantially smaller signal-to-noise ratio. The resolution of the dissipation data is similar to that of the current data.
24. Notably, the W tip is not an oriented single crystal but the apex of a polycrystalline W wire. The orientation of the tip was not known beforehand in our experiment. However, a tip that provides good STM images exposes a single W atom at the tip apex, and it is reasonable to assume that high-symmetry orientations provide stable tips. The geometry of the next neighbor atoms of the tip could be determined by field ion microscopy (FIM) (*44*), but space constraints prevent the implementation of FIM in our low-temperature AFM/STM.
25. G. K. Binnig, *Phys. Scr.* **T19**, 53 (1987).
26. W. A. Hofer, A. S. Foster, A. L. Shluger, *Rev. Mod. Phys.* **75**, 1287 (2003).
27. F. Ohnesorge, G. Binnig, *Science* **260**, 1451 (1993).
28. The atomic radii of W and C are taken as half the nearest neighbor distance in bulk W [bcc, cubic lattice constant 316 pm (*2*)] and graphite (142 pm), respectively.
29. E. Stoll, *Surf. Sci. Lett.* **143**, L411 (1984).
30. M. Herz, F. J. Giessibl, J. Mannhart, *Phys. Rev. B* **68**, 045301 (2003).
31. F. J. Giessibl, *Science* **267**, 68 (1995).
32. S. Kitamura, M. Iwatsuki, *Jpn. J. Appl. Phys.* **34**, L145 (1995).
33. T. R. Albrecht, P. Grutter, H. K. Horne, D. Rugar, *J. Appl. Phys.* **69**, 668 (1991).
34. R. Garcia, R. Perez, *Surf. Sci. Rep.* **47**, 197 (2002).
35. M. Lantz *et al.*, *Science* **291**, 2580 (2001).
36. U. Dürig, *Appl. Phys. Lett.* **76**, 1203 (2000).
37. F. J. Giessibl, S. Hembacher, H. Bielefeldt, J. Mannhart, *Science* **289**, 422 (2000).
38. M. Huang, M. Cuma, F. Liu, *Phys. Rev. Lett.* **90**, 256101 (2003).
39. M. Lantz *et al.*, *Phys. Rev. Lett.* **84**, 2642 (2000).
40. T. Eguchi, Y. Hasegawa, *Phys. Rev. Lett.* **89**, 266105 (2002).
41. T. R. Albrecht, C. F. Quate, *J. Appl. Phys.* **62**, 2599 (1987).
42. S. Hembacher, F. J. Giessibl, J. Mannhart, C. F. Quate, *Proc. Natl. Acad. Sci. U.S.A.* **100**, 12539 (2003).
43. S. Hembacher, F. J. Giessibl, J. Mannhart, data not shown.
44. H. W. Fink, *IBM J. Res. Develop.* **30**, 460 (1986).
45. We thank G. Binnig, M. Herz, and C. Quate for valuable discussions and comments and C. Quate for encouraging us to perform experiments on graphite. Supported by the Bundesministerium für Bildung und Forschung (project no. 13N6918).

29 April 2004; accepted 25 May 2004
Published online 10 June 2004;
10.1126/science.1099730
Include this information when citing this paper.

Electronic Transitions in Perovskite: Possible Nonconvecting Layers in the Lower Mantle

James Badro,[1]* Jean-Pascal Rueff,[2] György Vankó,[3] Giulio Monaco,[3] Guillaume Fiquet,[1] François Guyot[1]

We measured the spin state of iron in magnesium silicate perovskite $(Mg_{0.9},Fe_{0.1})SiO_3$ at high pressure and found two electronic transitions occurring at 70 gigapascals and at 120 gigapascals, corresponding to partial and full electron pairing in iron, respectively. The proportion of iron in the low spin state thus grows with depth, increasing the transparency of the mantle in the infrared region, with a maximum at pressures consistent with the D″ layer above the core-mantle boundary. The resulting increase in radiative thermal conductivity suggests the existence of nonconvecting layers in the lowermost mantle.

Heat can be transported in the mantle by conduction, radiation, or convection. Convection in the lower mantle is only initiated if the other two processes fail to transfer the heat flux produced from the secular cooling of the core and radioactive decay through the lower mantle, that is, if ratio of heat transport through convection to heat transport through conduction and radiation is high enough. Changes in the conduction or radiation properties of lower-mantle mineral assemblages will therefore strongly affect lower-mantle dynamics (*1–8*).

Earth's lower mantle is mainly composed (*9*) of iron-bearing magnesium silicate perovskite, $(Mg,Fe)SiO_3$, which is the most abundant phase (about 80% by volume), and magnesiowüstite, (Mg,Fe)O. Iron in magnesiowüstite undergoes a high-spin (HS) to low-spin (LS) transition between 60 and 70 GPa (*10*). Such changes can have effects on various properties, such as iron partitioning (*11*) or partial melting (*12*). But, one of the main and intrinsic characteristics of LS iron-bearing minerals resides in the blue shift (*11*, *13*) of iron absorption bands (the absorption bands initially in the infrared (IR) and red region shift to the green-blue region). Here, we show that $(Mg,Fe)SiO_3$, hereafter called perovskite, undergoes two such transitions at lower-mantle pressures. Therefore, both perovskite and magnesiowüstite should become increasingly transparent to red and IR radiation at depths between the bottom third of the mantle and the core-mantle boundary.

We probed the spin state and measured the spin magnetic moment of iron in $(Mg_{0.9},Fe_{0.1})SiO_3$ perovskite from 20 to 145 GPa by using high-resolution Kβ x-ray emission spectroscopy. The measurements were performed on the ID16 inelastic x-ray scattering beam line of the European Synchrotron Radiation Facility (ESRF). The details of the experimental setup (*14*) and sample preparation (*15*) are reported elsewhere. In order to release stresses and to avoid any presence of disordered or amorphous phases, we heated the sample with a neodymium: yttrium-aluminum-garnet (Nd:YAG) laser operating in TEM_{00} (single transverse) mode at each pressure point between 30 and 120 GPa. At higher pressures, laser radiation did not couple with the sample, and heating of the sample was not possible any more.

The spectra (Fig. 1A), which have been vertically shifted for clarity, reveal two transitions associated with a decrease of Kβ′ peak intensity (Fig. 2A) and shifting of the $K\beta_{1,3}$ peak to lower energy (Fig. 2B), occurring around 70 GPa and 120 GPa, respectively. The detailed description of the Kβ process is given elsewhere (*10*). The study of pressure-induced HS-to-LS transitions in geophysically relevant materials (*10*, *16–18*) has recently been possible thanks to the sensitivity of this technique. The emission spectrum

[1]Laboratoire de Minéralogie Cristallographie de Paris (UMR CNRS 7590), Institut de Physique du Globe de Paris, Université Paris, 6 and 7, 4 Place Jussieu, 75252 Paris, France. [2]Laboratoire de Chimie Physique–Matière et Rayonnement (UMR CNRS 7614), Université Paris, 6 11 Rue Pierre et Marie Curie, 75231 Paris, France. [3]European Synchrotron Radiation Facility (ESRF), B.P. 220 F-38043 Grenoble CEDEX, France.

*To whom correspondence should be addressed. E-mail: james.badro@lmcp.jussieu.fr

of HS iron is characterized by a main peak ($K\beta_{1,3}$) with an energy of 7058 eV and a satellite peak ($K\beta'$) located at lower energy as a result of the interaction of the core hole with the spin-polarized 3*d* shell (*15*). Because the LS state of iron is characterized by a lower-spin magnetic moment than the HS state, the eventual pairing of the electrons as a consequence of pressure increase leads to an intensity decrease of the $K\beta'$ peak (Figs. 1A and 2A), which is directly proportional to the relative abundance of the HS and LS species (Fig. 2A, right scale). Moreover, the energy shift of the $K\beta_{1,3}$ line (by −0.75 eV) measured in perovskite between 20 and 145 GPa (Fig. 2B) is consistent with predicted values for a HS-to-LS transition (and also linearly scales to the relative abundance of the species); indeed, the transfer of spectral weight to the satellite region in the HS state compared to the LS state, where the satellite is largely reduced, is balanced by a displacement of the main peak in the opposite direction in order to keep the center of mass of the emission line fixed (*19*). The pressure dependence of the iron magnetic state derived from the data analysis (Fig. 2) shows the two successive transitions at around 70 and 120 GPa. The evolution of our spectra up to 100 GPa is at odds with claims of a gradual transition in a recent study (*20*) performed up to that pressure; our measurements show a nearly constant $K\beta'$ peak intensity (Fig. 2A) and $K\beta_{1,3}$ peak position (Fig. 2B) as well as a similar line shape (Fig. 1A) for all spectra in a given spin state (HS, mixed state, or LS). Therefore, iron in a HS state at low pressure undergoes a first transition at 70 GPa to a "mixed" state (where a fraction of the iron goes to the LS state, the rest remaining in the HS state); at 120 GPa, a second transition occurs transforming the remaining HS iron to the LS state; above this pressure, all iron in perovskite is in the LS state. Support for our interpretation of the two transitions comes from a direct comparison [i.e., without fitting (Fig. 1B)] with reference spectra of molecular spin crossover compounds (*21*) containing ferrous or ferric iron in the HS and LS states (*15*).

Iron in perovskite can be in the ferrous (Fe^{2+}) or ferric (Fe^{3+}) valence state and can occupy one of two crystallographic sites (*22*). Although the exact partitioning behavior of ferrous and ferric iron between these two sites is poorly characterized, current interpretation (*22*) indicates that the large dodecahedral A site is the host of ferrous iron, whereas the smaller octahedral B site is the host of ferric iron together with lesser amounts of the ferrous species. In the conditions of synthesis and with 2 mole percent iron in our sample, perovskite contains about 75% Fe^{2+} and 25% Fe^{3+}, with 75% of the Fe^{2+} being in the A site and 25% in the B site and with all Fe^{3+} being in the B site (*22*). These values would lead to the following distribution of iron in perovskite: 56% ferrous dodecahedral, 25% ferric octahedral, 19% ferrous octahedral; i.e., 56% of total iron in the A site and 44% in the B site. The relative amounts of the HS and LS iron species in the mixed state are roughly 55% and 45%, respectively (Fig. 2, right scales), which indicates that the transitions could be site-specific; the first and second transitions could correspond to electron pairing in the A and B site, respectively. One should, however, not be deceived by this numerical coincidence; the technique used here is not highly sensitive to elemental proportions, and although the similarity of the figures could indicate it, we cannot at present ascribe the two transitions to the A and B sites.

Our sample was aluminum-free, which is known to increase the Fe^{3+}/Fe^{2+} ratio and to modify the compressibility (*23*–*25*) of perovskite. Similar experiments need to be performed on such systems in order to quantify the effect of aluminum on the spin transitions. Also, the effect of temperature will also need to be probed in order to transfer these laboratory observations to the real Earth system. If one assumes that the transition is density-driven (which spin transitions often are), the effect of temperature would consist in an increase of the transition pressure in order to counterbalance the thermal expansion term. The temperature correction could range from 15 GPa to 18 GPa between 70 and 120 GPa (*15*, *26*) at 2500 K, which can be considered as an average value

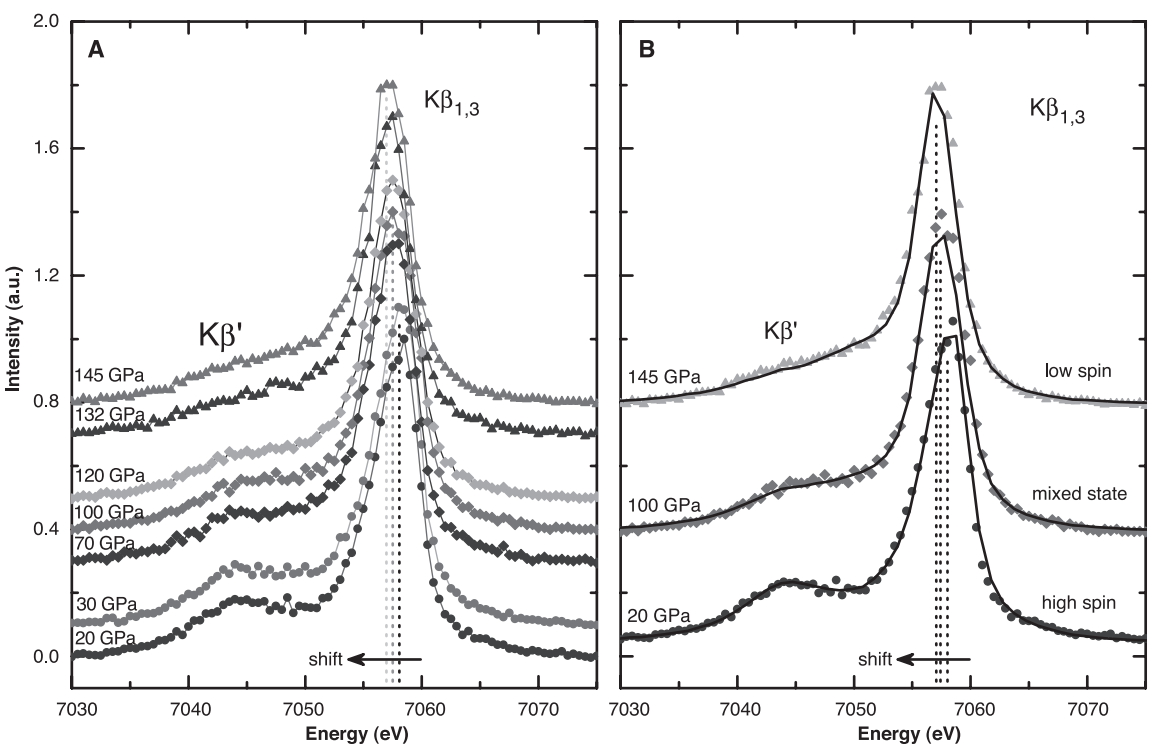

Fig. 1. (**A**) X-ray emission spectra collected on $(Mg_{0.9},Fe_{0.1})SiO_3$ between 20 and 145 GPa. The spectra have been vertically shifted for clarity. The presence of a satellite structure ($K\beta'$ line) on the low-energy side of the iron main emission ($K\beta_{1,3}$) line is characteristic of a HS 3*d* magnetic moment. The spin state of iron transforms twice at 70 and 120 GPa, as indicated by the changes in $K\beta'$ line intensity. Moreover, the position of the $K\beta_{1,3}$ line shifts with each transition (central position shown by the vertical dashed lines) and by a total of −0.75 eV between 20 and 145 GPa, which is in agreement with a HS-LS transition in iron. All spectra in a given spin state are similar in terms of both $K\beta'$ intensity and $K\beta_{1,3}$ position. (**B**) The solid lines are models (*15*) constructed from reference molecular compounds and are not fitted to the data. Three spectra taken from three different states (HS at 20 GPa, mixed state at 100 GPa, and LS at 145 GPa) are plotted on top to show the agreement. All of the individual spectra are available in color online (*15*).

for the deep lower mantle geotherm (*27*). This correction can also be estimated with the Clapeyron slope of the transition, which yields comparable values (*15*).

It was recently reported that perovskite undergoes a crystallographic phase transition at D″ conditions, in full accord with our second transition pressure. One can conjecture that the last electronic transition reported here is linked to (or could even be a driving force for) the phase transformation observed by Murakami *et al*. (*28*). Also, it was shown (*10*) that iron in magnesiowüstite undergoes a HS-LS transition at 70 GPa. Relying on theoretical studies that iron in perovskite remains in the HS state at geophysically relevant pressures, the study suggested on the basis of thermodynamic calculations that iron strongly partitions in the magnesiowüstite phase above this pressure. Here, we find that a similar yet incomplete transition occurs in the same pressure range in perovskite. This should reduce the magnitude of the partition coefficients previously proposed. With the two major lower-mantle minerals coexisting in various spin states, accurate theoretical modeling is needed to precisely quantify this issue; nevertheless, claims for a different thermochemical state of the lower mantle below 1700 km (*10*) are actually strengthened.

A HS-LS transition should increase the intrinsic radiative thermal conductivity of perovskite (*11*, *13*). Indeed, radiative conductivity in HS iron-bearing lower-mantle minerals is hindered by light absorption in the near-IR spectral region because of intraband transitions (*6*–*8*, *29*, *30*). A HS-LS transition of iron in these minerals is accompanied by a blue shift of these absorption bands from the near-IR to the visible (blue-green) spectrum, as has been shown for octahedral Fe^{2+}-bearing minerals (*11*), and is likely in the case of dodecahedral coordination (*15*). In turn, light with wavelengths in the red to near-IR spectral range should radiate through the assemblages with a longer mean absorption length. This spectral range corresponds to the maximum of blackbody emission for temperatures between 2000 K and 3000 K (970 nm at 3000 K), meaning that most of the radiative energy emitted from the core and lowermost mantle should be affected by the HS-LS transition (*15*). Our sample was heated with an IR laser at each pressure point in order to anneal the sample and to release stresses generated at such high pressures. Heating using the 1064-nm radiation of a Nd:YAG laser is achieved in metal-bearing silicates through the absorption by ligand field absorption bands (*31*); that energy is then converted to heat, and the technique has been used to reach temperatures in excess of 5000 K in the diamond anvil cell (*31*). However, above 120 GPa, when all the iron in perovskite transformed to the LS state, it was not possible to heat the sample with the radiation of the Nd:YAG laser (1064 nm) any more, and only the focused laser spot could be observed on the sample with a charge-coupled device (CCD) camera imaging system (*32*), as opposed to a bright heating spot when the laser couples at lower pressure. This provides an additional indication that, above 120 GPa, absorption by perovskite in the IR is hindered. Because this observation was made only after the second transition, we suggest that it has the most radical effect on IR absorption and hence on radiative heat transfer in perovskite.

The pressure range of the first transition (70 GPa) is consistent with the depth (1700 km) at which lower mantle chemical heterogeneities have been proposed (*33*) as well as with the transition pressure for iron in magnesiowüstite (*10*), the other main iron-bearing mineral of the lower mantle. The second transition pressure (120 GPa, corresponding to a depth of 2600 km), at which the HS-LS transition is completed in perovskite, is consistent with that of the D″ layer; at higher pressure (or below this depth), all lower-mantle minerals consist of LS iron. An important characteristic of this assemblage would be an increased radiative conductivity. The transitions should have a strong dynamical signature as inferred from geodynamical modeling (*2*, *4*–*5*), because an increase in thermal conductivity will result in a decrease of the Rayleigh number and hence may hinder convection and favor layering.

Recently, a thermal conductivity model of the mantle was derived from an extrapolation of spectroscopic data obtained at room pressure and temperature (*34*). Such models are not yet able to take into account the radical effects that spin-pairing transitions can have on the radiative term of thermal conductivity. Recent convection models (*4*–*5*) account for radiative conductivity on the basis of this model; if modified, it would allow to gauge the effects of the spin-pairing transitions on lower-mantle dynamics.

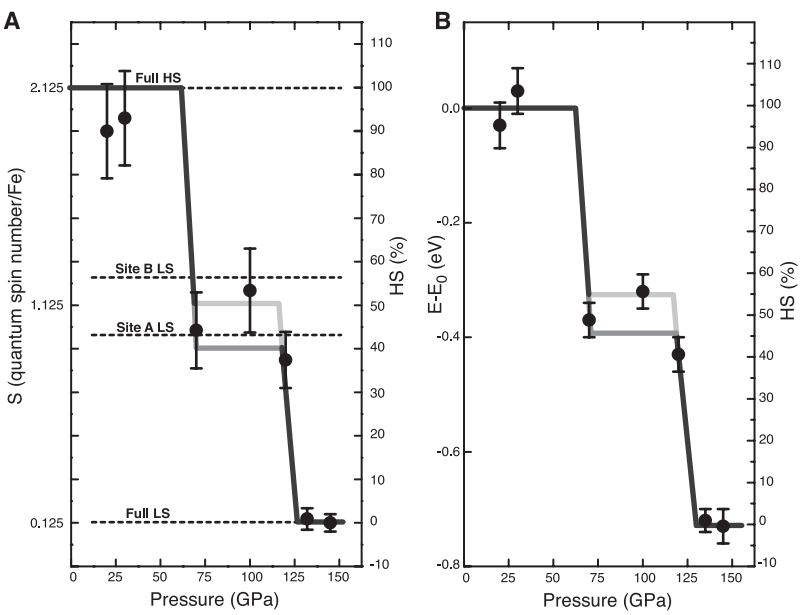

Fig. 2. (**A**) Average quantum spin number on the iron atom as a function of pressure, derived from the intensity of the Kβ′ line. It indicates that two transitions occur in perovskite at 70 and 120 GPa. The lines are guides to the eye. In the mixed state, the two curves represent upper and lower bounds of the iron magnetic moment. The corresponding abundance *x* of iron atoms in the HS state is represented on the right vertical axis, and the abundance of the LS atoms is (*1* – *x*). These values aim at showing that the two collapses could be consistent with site-specific transitions, because the proportion of HS and LS iron in each of the three regimes is consistent with the proportion of iron in the A and B sites. Because these latter values are very close (iron occupancy of the A and B sites differ by 10%), it is difficult to attribute a specific transition to a specific site within our error bars. (**B**) $K\beta_{1,3}$ line position as a function of pressure, showing again that the two transitions occur at 70 and 120 GPa. Note that the system evolves in three independent states: the HS state below 70 GPa, the mixed state between 70 and 120 GPa, and the LS state above 120 GPa.

References and Notes

1. G. F. Davies, in *The Earth's Mantle*, I. Jackson, Ed. (Cambridge Univ. Press, Cambridge, 1998), pp. 228.
2. L. H. Kellogg, B. H. Hager, R. D. van der Hilst, *Science* **283**, 1881 (1999).
3. P. Tackley, *Science* **288**, 2002 (2000).
4. F. Dubuffet, D. A. Yuen, *Geophys. Res. Lett.* **27**, 17 (2000).
5. A. P. van den Berg, D. A. Yuen, V. Steinbach, *Geophys. Res. Lett.* **28**, 875 (2001).
6. S. P. Clark Jr., *Trans. Am. Geophys. Union* **38**, 931 (1957).
7. T. Goto *et al*., *Phys. Earth Planet. Inter.* **22**, 277 (1980).
8. T. J. Shankland, U. Nitsan, A. G. Duba, *J. Geophys. Res.* **84**, 1603 (1979).
9. L. G. Liu, *Geophys. Res. Lett.* **2**, 417 (1975).
10. J. Badro *et al*., *Science* **300**, 789 (2003).

11. R. G. Burns, *Mineralogical Application of Crystal Field Theory* (Cambridge Univ. Press, Cambridge, 1993).
12. E. S. Gaffney, D. L. Anderson, *J. Geophys. Res.* **78**, 7005 (1973).
13. D. M. Sherman, *J. Geophys. Res.* **96**, 14299 (1991).
14. F. Sette *et al.*, *Phys. Rev. Lett.* **75**, 850 (1995).
15. See supporting data on *Science* Online.
16. J.-P. Rueff *et al.*, *Phys. Rev. B* **60**, 14510 (1999).
17. J. Badro *et al.*, *Phys. Rev. Lett.* **83**, 4101 (1999).
18. J.-P. Rueff *et al.*, *Phys. Rev. Lett.* **82**, 3284 (1999).
19. G. Peng *et al.*, *Appl. Phys. Lett.* **65**, 2527 (1994).
20. J. Li *et al.*, *Eos* **84** (suppl.), 46 (abstr. S21E-0376) (2003).
21. G. Vankó *et al.*, *ESRF Highlights* **2002**, 59 (2002); available online at http://www.esrf.fr/UsersAndScience/Publications/Highlights/2002/HRRS/HRRS9/
22. C. A. McCammon, *Nature* **387**, 694 (1997).
23. J. Zhang, D. J. Weidner, *Science* **284**, 782 (1999).
24. I. Daniel *et al.*, *Geophys. Res. Lett.* **28**, 3789 (2001).
25. D. Andrault, N. Bolfan-Casanova, N. Guignot, *Earth Planet. Sci. Lett.* **193**, 501 (2001).
26. P. Gillet *et al.*, *Phys. Earth Planet. Inter.* **117**, 361 (2000).
27. J. M. Brown, T. J. Shankland, *Geophys. J. R. Astron. Soc.* **66**, 579 (1981).
28. M. Murakami *et al.*, *Science* **304**, 855 (2004).
29. H. Keppler, C. A. McCammon, D. C. Rubie, *Am. Min.* **79**, 1215 (1994).
30. Q. Williams *et al.*, *J. Geophys. Res.* **95**, 21549 (1990).
31. R. Boehler, *Rev. Geophys.* **38**, 221 (2000).
32. The CCD camera is slightly sensitive in the IR, which allows imaging of the laser spot itself.
33. R. D. van der Hilst, H. Kárason, *Science* **283**, 1885 (1999).
34. A. M. Hofmeister, *Science* **283**, 1699 (1999).

Supporting Online Material
www.sciencemag.org/cgi/content/full/305/5682/383/DC1
Materials and Methods
SOM Text
Figs. S1 to S4
References and Notes

6 April 2004; accepted 10 June 2004

Structure and Flexibility Adaptation in Nonspecific and Specific Protein-DNA Complexes

Charalampos G. Kalodimos,[1]* Nikolaos Biris,[1]* Alexandre M. J. J. Bonvin,[1] Marc M. Levandoski,[2] Marc Guennuegues,[1] Rolf Boelens,[1] Robert Kaptein[1]†

Interaction of regulatory DNA binding proteins with their target sites is usually preceded by binding to nonspecific DNA. This speeds up the search for the target site by several orders of magnitude. We report the solution structure and dynamics of the complex of a dimeric *lac* repressor DNA binding domain with nonspecific DNA. The same set of residues can switch roles from a purely electrostatic interaction with the DNA backbone in the nonspecific complex to a highly specific binding mode with the base pairs of the cognate operator sequence. The protein-DNA interface of the nonspecific complex is flexible on biologically relevant time scales that may assist in the rapid and efficient finding of the target site.

Protein-nucleic acid interactions are responsible for the regulation of key biological functions such as transcription, translation, replication, and recombination. Understanding the mechanisms by which regulatory proteins discern their target sequences within the DNA genome requires that we also understand the properties of their complexes with nonspecific DNA (*1*). Nonspecific sites participate in the regulation of the physiological function because they complex, in vivo, most of the DNA binding protein molecules that are not bound at their regulatory functional sites (*2*). Furthermore, protein–nonspecific DNA interactions may also play an important role in the in vivo translocation of DNA binding proteins (*3*, *4*). Indeed, it has been demonstrated that proteins can find their DNA target sites at rates that are much faster than diffusion-controlled by initially binding to DNA anywhere along the chain and then translocating to their specific sites by a combination of intramolecular processes, including one-dimensional (1D) diffusion along the DNA (*5*–*7*). Most, if not all, proteins that interact with specific sites bind also nonspecifically to DNA with appreciable affinity. Thus, nonspecific interaction is an important intermediate step in the process of sequence-specific recognition and binding (*8*). Description of the structural and dynamic response of protein binding to both nonspecific and cognate operator sequences is a prerequisite for elucidating the physicochemical mechanisms that underlie the protein-DNA recognition process.

Many studies have revealed that sequence-specific binding is coupled to extensive conformational changes in both protein and DNA components (*9*, *10*). How does protein binding to nonspecific DNA, which precedes the specific binding, alter the structural and dynamic features of the partners? How does the complex switch from the nonspecific to the specific mode during the exploration process? These questions remain unanswered, mainly because of the scarcity of data on nonspecific binding. To address these central issues, we have structurally and dynamically characterized the DNA binding domain (DBD) of the lactose repressor in the free state and bound to a nonspecific DNA sequence and to its natural operator. *Lac* repressor, which is a prototype of transcription regulation, binds with a dimeric DNA binding unit to its cognate operator sequences 10^2 to 10^3 times faster than the rate estimated for a 3D diffusion-controlled reaction, with very high specificity (*11*). We previously reported the structure of the dimeric *lac* DBD free in solution and bound to its natural operator *O1* (*12*, *13*). Here, we report the high-resolution structure of the dimeric *lac* DBD bound to an 18-base-pair nonspecific DNA fragment (NOD). The variation of flexibility and the redistribution of the native-state ensemble along the recognition pathway were probed by relaxation and hydrogen-deuterium (H-D) exchange methodologies. The new findings also provide a molecular basis for explaining the thermodynamics of specific compared with nonspecific binding.

A dimeric *lac* headpiece-62 (HP62) mutant (*12*, *14*), which binds DNA with an affinity similar to that of the intact *lac* repressor, formed a stable and unique complex with an 18-base-pair-long nonspecific fragment (fig. S1) (*15*). The structure was determined on the basis of 2412 experimental restraints derived from multidimensional nuclear magnetic resonance (NMR) spectroscopy [Supporting Online Material (SOM) Text and table S1]. The ensemble of the 20 lowest-energy conformers is depicted in Fig. 1A.

Remarkably, the protein tilts by ~25°, relative to the DNA (Fig. 2A), compared to the specific complex, resulting in a dramatic alteration of the protein-DNA contacts (Fig. 2C). The side chains of Tyr^7, Tyr^{17}, Gln^{18}, and Arg^{22}, the primary residues that confer specificity to *lac* repressor through direct interactions with the base pairs in the major groove of the cognate operator (Fig. 2C) (*13*), shift and twist so as to participate in hydrogen bonds or electrostatic interactions with the phosphates (Figs. 1B and 2B). Consequently, a cavity is formed in the protein-DNA interface that can accommodate water molecules. In some of the structural conformers, these residues interact with the major groove through water bridges (SOM Text and fig. S3). A direct intermolecular hydrogen bond between the side chain of Tyr^{17} and the O2P phosphate atom of Thy^8 is present in all conformers. We tested the observed interaction of the Tyr^{17} hydroxyl group with the phosphate backbone by examining the DNA binding of a mutant repressor in which Tyr^{17} was mutated to Phe (Y17F) in the context of full-length *lac* repressor (SOM Text). For binding to the specific operator, removal of the Tyr^{17} OH

[1]Bijvoet Center for Biomolecular Research, Utrecht University, Padualaan 8, 3584 CH Utrecht, Netherlands. [2]Department of Biochemistry, University of Wisconsin-Madison, Madison, WI 53706, USA.

*Present address: Department of Chemistry, Rutgers University, Newark, NJ 07102, USA.
†To whom correspondence should be addressed. E-mail: kaptein@nmr.chem.uu.nl